# Rectifying jet breakup by electric forcing

David van Assche, Thomas Beneyton, Jean-christophe Baret

Received: 30 August 2022 | Accepted: 28 December 2022

DOI: 10.1002/dro2.45

RESEARCH ARTICLE

Droplet WILEY

# Rectifying jet breakup by electric forcing

David Van Assche[1] | Thomas Beneyton[1] | Jean-Christophe Baret[1,2]

[1]CRPP, UMR5031, CNRS, Université de Bordeaux, Pessac, France

[2]Institut Universitaire de France, Paris, France

**Correspondence**
Jean-Christophe Baret, CRPP, UMR5031, CNRS, Université de Bordeaux, 115 Ave Albert Schweitzer, Pessac 33600, France.
Email: jean-christophe.baret@u-bordeaux.fr

**Funding information**
Région Nouvelle Aquitaine; The European Union's Horizon 2020 Research and Innovation Program under the Marie Sklodowska-Curie, Grant/Award Number: 813786

## Abstract

The high-throughput production of monodisperse droplets is paramount in most of the applications in droplet microfluidics. In a flow-focusing junction, a straightforward way to increase droplet production rate is to increase the flow rates. However, at a critical flow velocity, the droplet monodispersity breaks down due to a transition from the dripping to the jetting regime. As a result, a much more polydisperse droplet population is generated. The change from monodisperse to polydisperse droplet production emerges from the intrinsic properties of the instabilities of jets. In the jetting regime, droplet pinch-off is governed by a convective instability which amplifies random noise when traveling down the jet leading to an irregular breakup. We show that with the use of an amplitude-modulated electric signal, we select the breakup frequency of the jet. Matching the perturbation frequency close to the natural breakup frequency of the jet, we increase the monodispersity of the droplet population. This method is applicable to droplet production at a high throughput, that is, beyond the dripping to jetting threshold, including an active control since the frequency, and hence droplet sizes, are determined by the forcing frequency.

## INTRODUCTION

Droplet-based microfluidics is a technology used in a wide range of applications, including functional and genomic single-cell analysis,[1,2] protein engineering,[3,4] synthetic biology,[5–7] drug screening,[8,9] and material synthesis.[10–12] The technology relies on the production of monodisperse emulsions. Several microfluidic systems for droplet production exist co-flow,[13] T-junction,[14] step emulsification,[15,16] flow-focusing.[17–19] A flow-focusing junction is advantageous due to its simplicity and its compatibility with high throughput (typically ~$10^3$–$10^4$ per second for ~10–100 pl droplets[3,20,21]). In the flow-focusing geometry, one fluid is hydrodynamically focused by another immiscible fluid (Figure 1a). Capillary forces at the interface resist deformation, while inertial forces and viscous stresses promote the deformation of the interface. The competition between these forces, which together with the geometry of the junction make up the local flow field, leads to droplet pinch-off. For a given channel geometry, a straightforward way to increase the droplet production rate is to increase the flow velocities in the channel. However, the balance of viscosity, inertia, and capillarity is eventually changed, and the flow regime transitions from dripping to jetting.[22,23] This transition happens when the capillary number $Ca$, comparing the relative weight of capillary forces and viscous drag, and/or the Weber number $We$, comparing the relative weight of inertia and capillary forces, exceed their respective threshold value. In a nutshell, when dripping occurs ($Ca, We \lesssim 1$), droplets are formed periodically close to the junction resulting in uniform droplet size. At higher flow velocities, a jet is formed ($Ca \geq 1$ or $We \geq 1$), which eventually breaks up into droplets downstream of the nozzle due to the Plateau–Rayleigh instability.[24,25] Both regimes differ in terms of the stability of liquid threads.

In linear stability analysis of a liquid jet, the dripping regime has been related to an absolute instability[22,23,26–28]: perturbations grow and propagate from a fixed location both upstream and downstream

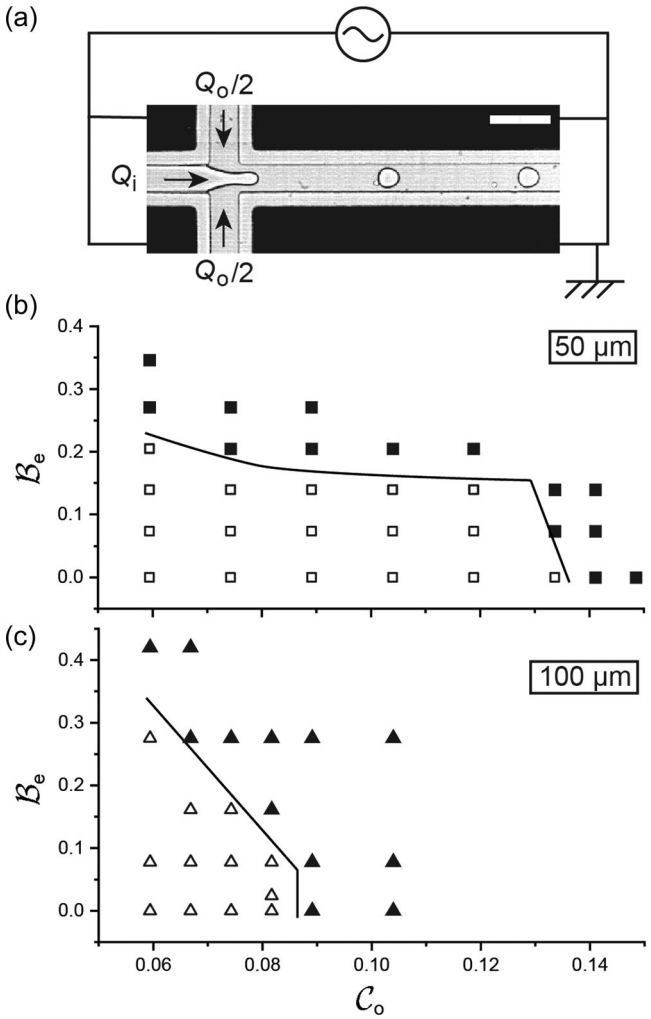


**FIGURE 1** Microfluidic device characterization. (a) Micrograph of the flow-focusing junction with a schematic of the electrode connections. The dark regions on the micrograph are the electrodes. The upstream electrodes can be actuated by a frequency generator while the downstream electrodes are grounded. The scale bar is 100 µm. (b, c) Dripping-to-jetting transition at the flow focusing junction rescaled to the dimensionless capillary number $\mathcal{C}_o$ and electric bond number $\mathcal{B}_e$ with $Q_i$ at 50 µl/h. The lines are a guide to the eyes for the dripping-to-jetting transition. (b) The nozzle size is 50 µm × 50 µm × 34 µm. (c) The nozzle size is 100 µm × 100 µm × 68 µm.

of the interface leading to monodisperse droplets produced at a rate that is intrinsic to the system. Absolutely unstable jets have been only rarely observed.[26] In contrast, the jetting regime is related to a convective instability: due to high flow velocities, instabilities propagate solely downstream of the interface while they grow. Random noise is amplified by the perturbations as they travel along the jet surface, resulting in less uniform droplet size. Therefore, the production rate of a monodisperse emulsion in a flow-focusing device is limited by the onset of the jetting regime where polydisperse emulsions are generated.

Imposing external perturbations on a jet, either mechanical[29] or by radiation[30] has been demonstrated to alter the breakup dynamics of a jet. For sufficient perturbation amplitude within a certain frequency range, the droplet pinch-off frequency of the jet is forced by the external perturbation frequency, suggesting an increase in the monodispersity of the droplet population. In this respect, electric fields may offer a way to impose local and precise perturbations compatible with integration in microdevices and fast response. Electric actuation of a jet has been applied in systems for microfabrication by electrospraying and electrospinning.[31] Pulsed electric fields were demonstrated for on-demand droplet production in an electrospinning configuration.[32] Electric actuation has also been shown to be a method that offers a fast way to affect the behavior at the flow-focusing junction. Electrowetting was used at the flow-focusing junction to manipulate the droplet production rate in the dripping regime.[33] When the electrodes are not in contact with the fluids, electric fields also offer a way to manipulate the droplet production regime.[34,35] With insulated electrodes around a flow-focusing junction, it was demonstrated that AC electric fields induce the jetting regime depending on the properties of the system and the electric field.[36,37] Therefore, the electric actuation of a jet may offer a way to perturb a jet and produce a monodisperse emulsion at high throughput.

Here, we present a method that uses amplitude-modulated electric fields to actively control the jet breakup. We show that the electric field provides a fast and simple way to impose perturbations on a hydrodynamic jet. We analyze the effect of different components of a modulated electric field (amplitudes, frequency) on the jet breakup, and we find that the modulation frequency of the electric field leads to an increase in monodispersity of the produced droplets at rates close to 10 kHz.

## RESULTS AND DISCUSSION

We use a standard droplet-based microfluidics flow-focusing junction with electrodes manufactured symmetrically around the junction (Figure 1a and Supporting Information: Figure S1).[34] We first study the dripping-to-jetting transition in the device as a function of the applied voltage $U_0$ across the electrodes. We fix the inner flow rate ($Q_i$) to a constant value of 50 µl/h and vary the outer flow rate ($Q_o$) to increase the viscous stress on the interface. We define $\mathcal{C}_o = \eta u/\gamma_0$ as the outer capillary number[22] where $\gamma_0$ is the surface tension, $u$ and $\eta$ the mean velocity and viscosity of the outer fluid. We further define the outer Reynolds number $\mathcal{R}_o = \rho u L/\eta$ and the outer Weber number $\mathcal{W}_o = \rho u^2 L/\gamma_0$, with $\rho$ the density and $L$ the typical length scale of the microchannel. The onset of the jetting regime is observed at $Q_o$ = 950 µl/h ($\mathcal{C}_o$ = 0.14; $\mathcal{R}_o$ = 0.21; $\mathcal{W}_o$ = 0.03), consistent with the dripping-to-jetting transition in capillaries.[23] The transition threshold is then measured for different applied voltages $U_0$. The threshold $Q_o$ decreases with increasing voltages. No dripping is observed for voltages above 220 V.

It has already been demonstrated that electric fields affect the droplet sizes in the dripping regime and induce jetting transition.[34] The electric field reduces to an interfacial contribution, neglecting

other effects such as the electro-osmotic flows. The Maxwell stress at the boundary of materials of different dielectric constant reduces the surface tension, according to the electrocapillary equation.[38]

$$\gamma = \gamma_0 - \frac{\varepsilon_0 \varepsilon_r U_0^2}{r}, \quad (1)$$

where $\gamma_0$ and $\gamma$ are the initial and resulting surface tension, $\varepsilon_0$ and $\varepsilon_r$ are the vacuum permittivity, and the relative permittivity of the oil phase and $r$ is the typical spacing of the electric capacitor formed by the electrodes. The electrocapillary equation provides a dimensionless number representing the balance of electric stress and surface tension in the form of the electric Bond number $\mathcal{B}_e = \varepsilon_0 \varepsilon_r U_0^2 / \gamma_0 r$. Here, $r$ is chosen as the distance between the upstream and downstream electrodes, which gives the typical dimension of the problem. We want to point out that the effective voltage at the fluid tip is not exactly the one applied since the equivalent electric circuit is modeled as a high-pass filter.[34] The exact value of the transition in $\mathcal{B}_e$ will therefore depend on the voltage loss. Here, we estimate that the voltage at the tip is 0.7 times the applied voltage, using the electric model presented by Tan et al.,[34] the value of 0.7 is a constant in our experiments for fixed a frequency of 30 kHz and fixed fluid properties. The dripping-to-jetting transition, therefore, occurs when one of the two numbers becomes larger than a threshold: $\mathcal{C}_o \gtrsim 0.14$ or $\mathcal{B}_e \gtrsim 0.20$ (Figure 1b).

Interestingly here, one can notice the analogy in the flow diagram with the inertial case.[23] Yet, the electric field provides an orthogonal means to control the dripping-to-jetting transition while keeping fixed hydrodynamic conditions.

We then test the robustness of these results by up-scaling the dimensions of the system. We double all the dimensions to obtain a nozzle size of 100 µm × 100 µm × 68 µm and repeat the experiment while keeping $Q_i$ at 50 µl/h (Figure 1c). In general, the shape of the flow diagram is unchanged, with a dripping region at small $\mathcal{C}_o$, $\mathcal{B}_e$, and a jet otherwise. The transition values are, however, modified. Without an electric field, we find the onset of the jetting regime at $Q_o$ = 2400 µl/h ($\mathcal{C}_o$ = 0.085; $\mathcal{R}_o$ = 0.27; $\mathcal{W}_o$ = 0.024). At the lowest $Q_o$ tested, the threshold value for dripping to jetting was $\mathcal{B}_e \approx 0.3$). Although $\mathcal{C}_o$ and $\mathcal{B}_e$ are the dimensionless numbers controlling the transition, the threshold values of $\mathcal{B}_e$ and $\mathcal{C}_o$ for the dripping-to-jetting transition are affected by the dimensions of the channel, and possibly by the flow rate ratio of both phases.

In summary, while the universality of the transition lines in the presence of an electric field would deserve a follow-up study, the flow diagram obtained for channels of 50 µm width fully characterizes the system that we will further study.

In the second part, we focus on the monodispersity of production, both in the dripping and in the jetting regime. We work with the 50 µm device. To measure the monodispersity of droplets over large populations (typically $4 \times 10^4$ droplets), we use a method based on fluorescence. A 473 nm laser spot is focused in the center of the channel downstream of the nozzle, and 200 µM of fluorescein is added to the aqueous phase. A photomultiplier tube (PMT) converts the emitted light from the fluorescent drops to a recorded electric signal $s(t)$. Each droplet appears as a peak in the time series $s(t)$. The frequency of the signal directly relates to the monodispersity of the droplet production. We compare the droplet formation in the dripping ($Q_o$ = 600 µl/h, Figure 2a) and the hydrodynamic jetting regime ($Q_o$ = 1200 µl/h, Figure 2b) in the absence of an electric field. In the dripping regime, droplet pinch-off happens close to the nozzle, while in the jetting regime, the droplet is pinched off further downstream away from the nozzle. Figure 2e,f shows the signal acquired by the PMT for ~80 consecutive droplets in both regimes. Figure 2i,j shows the amplitude of the fast Fourier transform (FFT) of a 5-s recording of the PMT signals (~$4 \times 10^4$ droplets) $F(f) = |\mathrm{FFT}[s(t)]|$. The PMT signal is very homogeneous, which results in one peak in the frequency spectrum $F(f)$ (Figure 2e,i). We recover here that the droplet production in the dripping regime results in a highly stable droplet production. In contrast, droplet production in the jetting regime results in a more heterogeneous PMT signal which results in a broader spectrum of the Fourier transform without a specific peak (Figure 2f,j). With our method, we recover here the main features of the absolute and convective instabilities, namely a well-defined frequency on the one hand and a broad range of amplified frequencies of perturbations on the other hand.

We now actuate the upstream electrodes to apply an electric field to the same hydrodynamic jet ($U_0$ = 300 V, $Q_o$ = 1200 µl/h). Figure 2c,g,k shows the corresponding micrograph, PMT signal, and frequency spectrum. Although $\mathcal{B}_e \gtrsim 0.20$, we do not observe any notable difference in the frequency spectrum as compared to the case of jetting in the absence of an electric field. Electrified jets have been shown to display a shift of the amplified perturbations toward higher frequency for inertial jets.[39] The absence of a similar shift in our experimental data might originate from viscous dissipation, which changes the dispersion relation, although no detailed calculations of the problem have been found in literature—to the best of our knowledge. At this step, we would nevertheless conclude from the experimental data that the electric field does not significantly alter the dynamics of the jetting. However, the jet behavior changes drastically when we move from a constant AC electric voltage to a modulated voltage.

We now apply an amplitude modulation at a fixed frequency in the range of the amplified frequency of the jet. This modulation acts at the interface as a perturbation of fixed frequency through the modulation of the Maxwell stress. We note $f_{pert}$ as perturbation frequency (here $f_{pert}$ = 8 kHz), and the maximum amplitude of the applied voltage is defined as $A_{pert}$ (here $A_{pert}$ = 300 V). The PMT signal of the forced jet shows a higher level in the homogeneity of amplitude compared to the unforced jets (Figure 2h), and the Fourier transform shows a clear peak at $f_{pert}$ = 8 kHz while the amplitude of the other frequencies is slightly decreased compared to unforced jets (Figure 2l). The modulation of the applied voltage is, therefore, a means to select a frequency among the frequency naturally amplified in the growth dynamics of perturbed jets to increase the monodispersity of jetting.

To further understand the properties of the jet instability, we further use the control that electric actuation easily provides, namely,

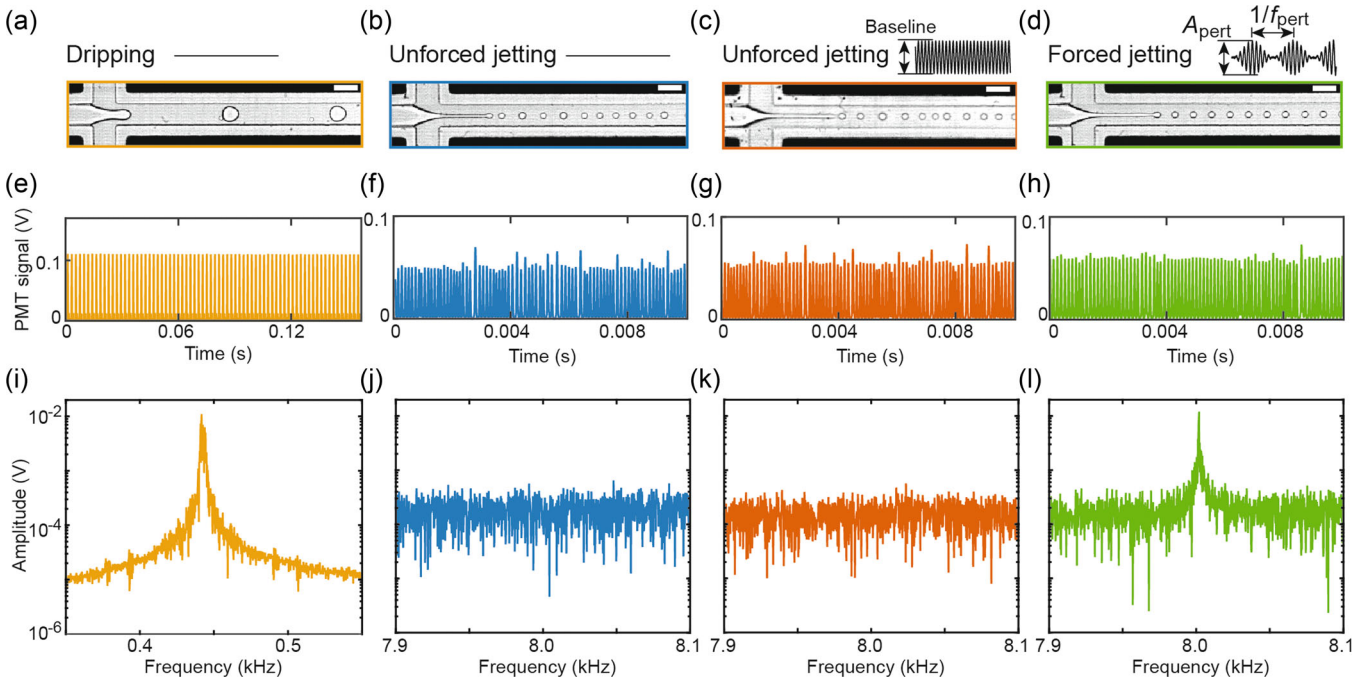


**FIGURE 2** Comparison of dripping, unforced, and forced jetting. (a–d) Micrographs of the different regimes with a sketch of the applied electric field. The scale bar is 50 µm. (e–h) Segment of the recorded photomultiplier tube (PMT) signals corresponding to the different regimes. (i–l) Fourier transform of a 5 s recording of the PMT signals. Yellow: $Q_o$ = 600 µl/h, no electric field; blue: $Q_o$ = 1200 µl/h, no electric field; orange: $Q_o$ = 1200 µl/h, baseline = 300 V; green: $Q_o$ = 1200 µl/h, $A_{pert}$ = 300 V, $f_{pert}$ = 8 kHz.

amplitude and frequency controls. We investigate the effect of the different components of the amplitude modulated (AM) signal (perturbation amplitude $A_{pert}$, perturbation frequency $f_{pert}$, and baseline voltage) on the jet breakup.

First, we look into the effect of $A_{pert}$ by setting $f_{pert}$ to 8 kHz and baseline to 0 V while stepwise increasing $A_{pert}$ from 0 to 300 V. The Fourier transform of the sequential PMT recordings are shown in Figure 3a and Supporting Information: Figure S3a–c. Here the grayscale represents the amplitude of the Fourier transform. We observe that with increasing $A_{pert,}$ the intensity at $f_{pert}$ increases while the intensity of other frequencies slightly decreases. To quantify this observation, we separate the power spectrum $F(f)$ into two separate signals as shown in Equation (2): (i) a $\delta(f_{pert})$ peak of amplitude $a_p$ at $f_{pert}$ and (ii) a background signal $F_0(f)$ spanning the frequency range corresponding to the power spectrum of the unperturbed jet ($A_{pert}$ = 0 V) with an amplitude $a_0$.

$$F(f) = a_0 F_0(f) + a_p \delta(f_{pert}), \tag{2}$$

where $a_0$ and $a_p$ are the parameters to be fitted, representing the intensity of both signals in the power spectrum. Figure 3b,c presents the evolution of $a_0$ and $a_p$ for the amplitude sweep. $a_0$ decreases while $a_p$ increases with $A_{pert}$.

This experiment is repeated with additional baseline voltages up to 500 V to investigate the effect of a baseline voltage on the jet breakup (Supporting Information: Figures S3 and S4). A faster increase of $a_p$ and a faster decrease of $a_0$ is observed in Figure 3b when applying a baseline voltage. We argue that applying a baseline voltage results in a charged jet that is more stable against perturbations than an uncharged jet. However, for high $A_{pert}$ and a baseline of 500 V $a_p$ decreases while $a_0$ increases. This is because the jet behavior suddenly transits under the influence of the high electric field. The jet widens and is pulled further down the channel.

We finally confirm that the analysis indeed corresponds to improved monodispersity using a second measurement of the monodispersity. In this case, we analyze the signal $s(t)$ to detect the peaks in the PMT signal corresponding to droplets. We then calculate a normalized histogram of the peak width. Afterward, a Gaussian curve with variables mean $\mu$ and standard deviation $\sigma$ is fitted to the histogram (Supporting Information: Figures S5–S7). Here, the standard deviation is a measure of the spread of the histogram, that is, a measure of the uniformity in droplet size. We rescale the resulting $\sigma$ to $\sigma_0/\sigma$, where $\sigma_0$ is the standard deviation at $A_{pert}$ = 0 V (Figure 3d). This means if $\sigma_0/\sigma > 1$, the size distribution of the droplet size is more uniform than the initial droplet population of an unperturbed jet. We observe that when $A_{pert}$ is sufficiently large $\sigma_0/\sigma$ increases and that this increase happens faster when a baseline voltage is applied. The maximum $\sigma_0/\sigma$ observed here is 3.5, meaning that the standard deviation of the droplet width is decreased 3.5 times compared to the standard deviation of an unperturbed jet. This method confirms that the emergence of the peak in the power spectrum indeed corresponds to a gain in monodispersity through the selection of the most amplified frequency.

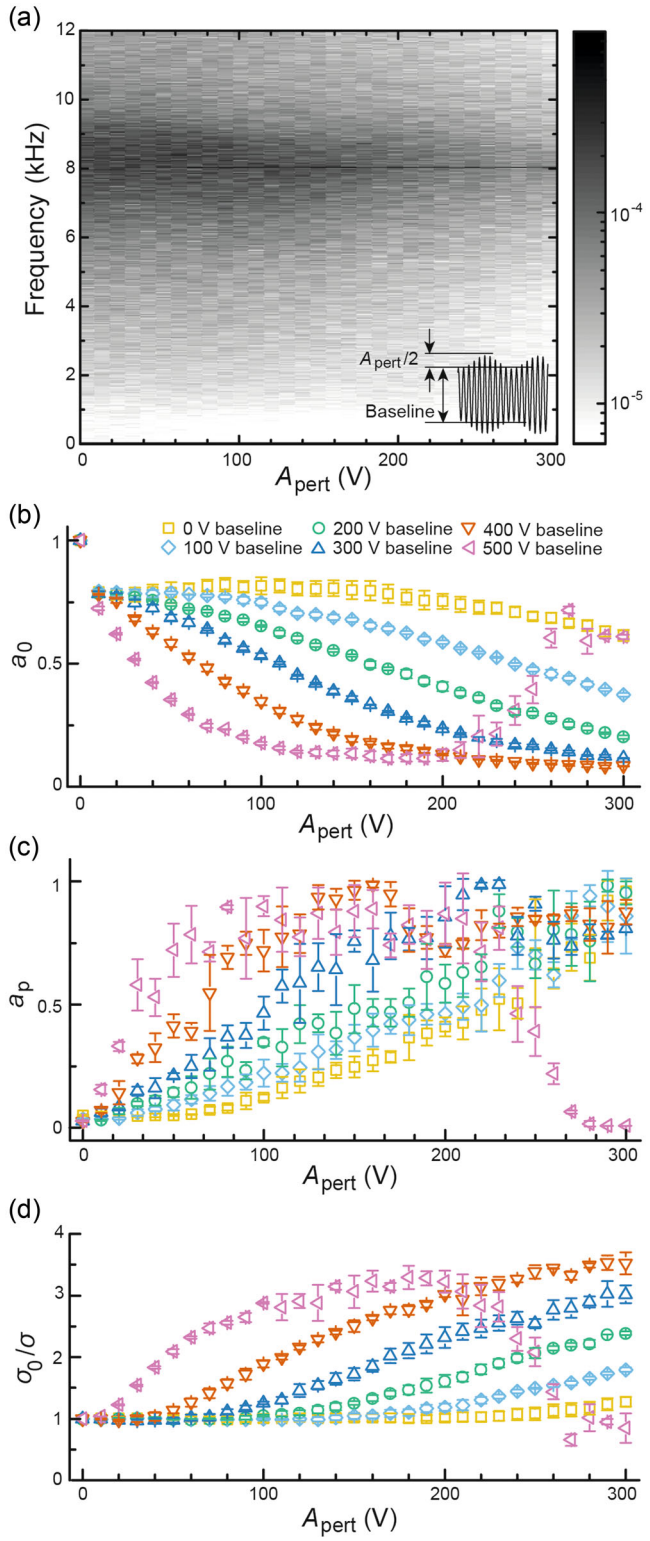


**FIGURE 3** Effect of $A_{pert}$ and baseline voltage on the jet breakup. $f_{pert}$ is set to 8 kHz. (a) Fourier transform of one sweep of the perturbation amplitude (baseline = 200 V). The grayscale corresponds to the amplitude of the Fourier transform. (b, c) Deconvolution of the Fourier transform into (b) a background and (c) a peak signal. (d) $\sigma_0/\sigma$ of the Gaussian curve fitted to the histogram of peak widths. Error bars show the standard deviation.

Finally, the effect of $f_{pert}$ on jet breakup is investigated. We set $A_{pert}$ to 200 V and varied $f_{pert}$ from 0 to 12 kHz for a baseline voltage of 0 and 200 V (Supporting Information: Figure S8). Figure 4a shows the Fourier transform of one such experiment. In Figure 4b, we again deconvolve the Fourier transform as in Equation 2. $a_0$ changes only slightly for low $f_{pert}$. For the frequencies around the natural breakup frequency of the jet (±8 kHz) we see a clear decrease in the background signal. At higher perturbation frequencies (>10 kHz), the effect of the AM signal on the background signal disappears.

For $a_p$, we observe an initial increase at ±1 kHz, which can also be seen in Figure 4a. Here the time to replenish the whole jet volume is matching the forcing frequency, that is, $f_{pert} \approx Q_i/V_{jet}$. The jet breaks up into one big and a train of smaller droplets, as can be seen in Figure 4d at $f_{pert} = 1$ kHz. This regime corresponds to observations of the production of groups of droplets under the influence of the electric field in the dripping regime.[40] A second increase of $a_p$ is seen around 8 kHz, the natural production frequency of the jet, where $a_0$ decreases. This means that when $f_{pert}$ is around the natural breakup frequency of the jet, it is amplified, while the other frequencies in the spectrum are reduced. For higher $f_{pert}$ the peak intensity decreases since the perturbations are too fast for the jet to follow.

In Figure 4c, $\sigma_0/\sigma$ of the peak width distribution is shown. Initially, a decrease in uniformity is observed for low $f_{pert}$. This is due to the breakup of the jet in clumps as stated earlier. The first peak for $a_p$ at 1 kHz corresponds to a decrease in monodispersity. Around the natural jet frequency of 8 kHz, $\sigma_0/\sigma$ increases showing a higher level of monodispersity ($\sigma_0/\sigma > 1$). For higher frequencies, the effect of the perturbations disappears ($\sigma_0/\sigma \approx 1$).

In Figure 4d, we aligned micrographs of the jet perturbed at different frequencies. Every fifth drop is colored red for visualization purposes. For lower frequencies, we see the disrupting effect of the perturbations. Further, we see that from 7 to 9 kHz, the distance between the drops decreases in a controlled fashion. This observation is validated in Supporting Information: Figure S9, where we see a steady decrease in the fitted parameter $\mu$ between 7 and 9 kHz. Altogether, this suggests that we can control the droplet production frequency of the jet around the natural breakup frequency without changing flow properties.

Modeling the electrohydrodynamic instability of the jet in confinement is a complex problem. However, as a qualitative statement, we calculate the frequencies which are amplified by the jet following the dispersion relation. From the Plateau–Rayleigh instability, we know that unstable modes for the breakup of a jet are $k \cdot r_{jet} < 1$ with $k$ the wavenumber and $r_{jet}$ the radius of the jet. Or, $\pi \cdot d_{jet} < \lambda$ with $d_{jet}$ the diameter of the jet and $\lambda$ the wavelength. We know that the relation between wavelength $\lambda$, velocity $U_{jet,}$ and frequency $f$ is $\lambda = U_{jet}/f$. We know that $U_{jet} = \frac{4Q_i}{\pi \cdot d_{jet}^2}$ for a cylindrical jet which gives $f < \frac{4Q_i}{\pi^2 \cdot d_{jet}^3}$. For $Q_i = 50$ µl/h and $d_{jet} = 7.8$ µm estimated from micrograph images, we find $f < 11.9$ kHz. Next to that,

theoretically, the frequency with the highest growth rate is $k \cdot r_{jet} = 0.697\lambda$ which results in $f_{max} = 8.3$ kHz. These findings correspond well to Figure 4d, where we find a peak in monodispersity around 8 kHz, and the effect of the perturbations disappears when $f_{pert}$ is greater than 11 kHz.

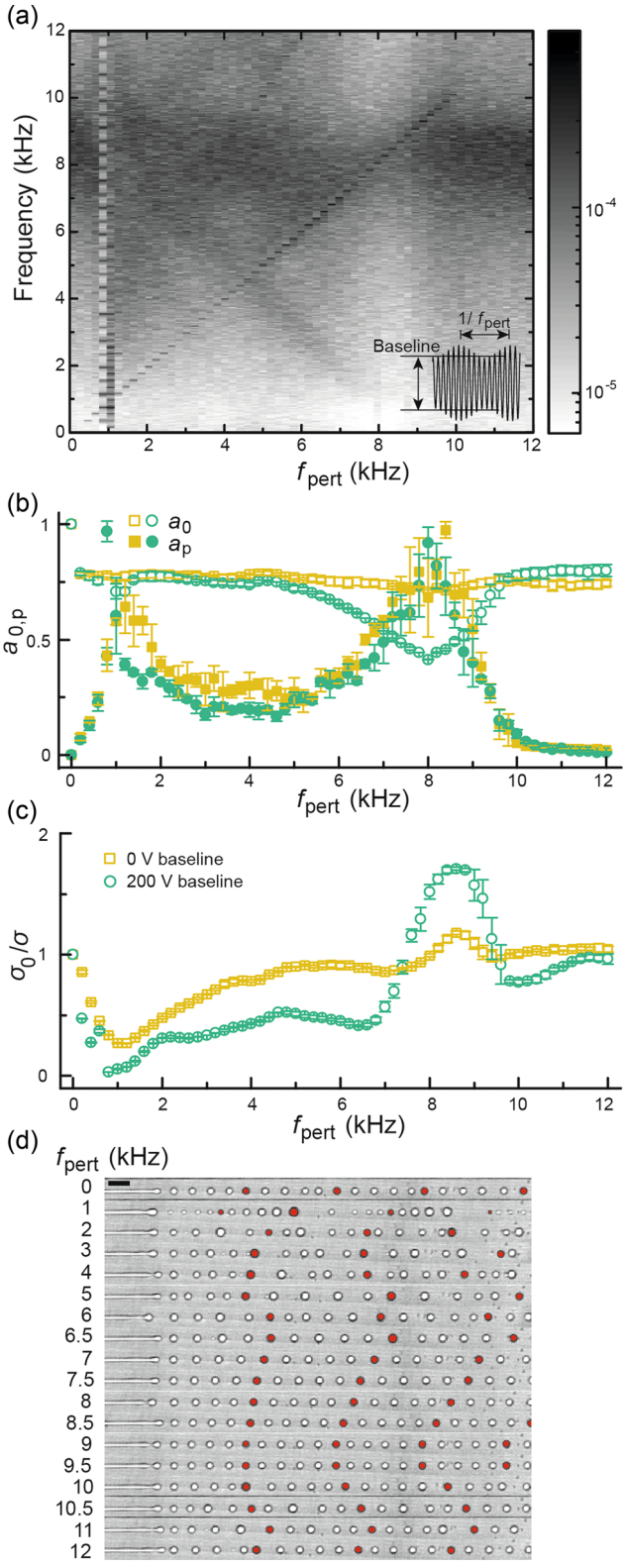


## CONCLUSION

In brief, we investigated the possibility of altering the breakup dynamics of a hydrodynamic jet in a flow-focusing junction by electric fields. We first observed that the onset of the jetting regime is affected by the electric field. This, however, did not alter the breakup dynamics significantly. We then modulated the amplitude of the electric field, which allowed us to rectify the jet, that is, there was a correlation between the modulation frequency and the breakup frequency of the jet. We further used the parameters of the electric field, to understand the jet instability. Tuning the electric parameters, we were able to increase the monodispersity of the drop population produced by the jet.

In our system, the capillary forces dominate over the viscous forces ($\mathcal{C} < 1$) and inertial forces ($\mathcal{W} \ll 1$). Inertial forces are small compared to viscous effects as we work with viscous liquids ($\mathcal{R}_o < 1$). The electric stress is small compared to the capillary stress ($\mathcal{B}_e < 1$). For the highest perturbation amplitude of 300 V, we find $\mathcal{B}_e \approx 0.32$, and for a baseline of 500 V, we find $\mathcal{B}_e \approx 0.84$.

We recover the traditional approximation that applied voltages act as an interfacial tension term: applying a baseline voltage reduces the equivalent surface tension by the Maxwell stress, and, thereby relatively reduces the capillary effects compared to inertial and viscous effects.

The volume of droplets produced at 8 kHz is 1.7 pl ($V = Q/f$). Production of such small droplets in the dripping regime using a flow-focusing junction is not easy to implement in the general case. Scaling down the geometry of the nozzle increases the probability of clogging the nozzle in practical applications prohibiting the reliable production of a monodisperse emulsion. Moreover, the pressure in the fluidic channels increases, which means it is necessary to operate at low flow velocities.

The droplets produced in our system are made with a viscous liquid ($\eta = 26.6$ mPa·s), for which we show that monodisperse emulsion can be generated at rates up to 8 kHz. However, in most applications, the viscosity of the aqueous phase is around 1 mPa·s. Here, we used a higher viscosity to be able to create a hydrodynamic jet without using surfactants. Interfacial instabilities grow more quickly in less viscous jets due to decreased viscous dissipation.

Because we wanted to control the interfacial properties of our system, we did not use surfactants in the experiments to avoid the

**FIGURE 4** Effect of $f_{pert}$ on the jet breakup. $A_{pert}$ is set to 200 V while $f_{pert}$ is stepwise increased. (a) Fourier transform of one sweep of the $f_{pert}$ with baseline = 200 V. The grayscale corresponds to the amplitude of the Fourier transform. (b) Deconvolution of the Fourier transform into a background (open symbols) and a peak signal (filled symbols). Yellow: baseline = 0 V; green: baseline = 200 V. Error bars show the standard deviation. (c) $\sigma_0/\sigma$ of the Gaussian curve fitted to the histogram of peak widths. $\sigma_0$ corresponds to the standard deviation of an unperturbed jet ($f_{pert} = 0$). Yellow: baseline = 0 V; green: baseline = 200 V. Error bars show the standard deviation. (d) Micrograph images at different $f_{pert}$. The first droplet of each image is aligned, while every fifth droplet is colored red. The scale bar represents 50 µm.

effect of the dynamic adsorption/desorption of the molecules at the interface, which introduces an additional level of complexity.[41,42] However, in practical applications, surfactants are used to avoid droplet coalescence. They decrease the surface tension resulting in an earlier onset of the jetting regime compared to no surfactants. In the long run, it will be important to determine to what extent the use of surfactants affects the generalization of the results obtained here.

In addition, while this study focuses on one specific formulation, the conductivity of the aqueous phase can also affect the generalization of the method.[34] However, we provide here a basic method used to control microcompartment creation alleviating the limitations observed when attempting to increase the throughputs of productions and going beyond other actuation mechanisms by light or acoustic radiations.[43,44] We believe that this approach is of interest for applications requiring high throughput and reliability in production, for example, in biomicrofluidics technologies and material sciences.

## METHODS

The microfluidic devices are fabricated using standard soft lithography methods.[45] A photoresist mold is manufactured on a silicon wafer (Si-Mat) by UV exposure using a mask aligner (MJB4; SUSS MicroTech). A spin-coated layer of photoresist (SU-8 3025; MicroChem) is selectively exposed by a photolithography mask (Selba; Supporting Information: Figure S1a) and subsequently developed (SU-8 Developer; MicroChem). Poly-dimethylsiloxane (PDMS; Sylgard 184) is mixed with a curing agent (Dowsil 184 Silic Elastomere Curing Agent) to a final concentration of 10% (w/w). After degassing using a vacuum pump, the PDMS mixture is poured onto the mold and incubated overnight at 70°C. The PDMS is peeled off, and the inlets and outlets are punched using a biopsy puncher. The PDMS chips are bonded onto the nonconducting side of an Indium Tin Oxide coated glass slide (Corning) using an oxygen plasma cleaner (Pico, Diener electronic). Before use, the channels are hydrophobized using Aquapel (PPG Industries). The dimension of the flow-focusing junction is 50 µm × 50 µm × 34 µm, as measured by a 3D optical microscope (Supporting Information: Figure S1b; Contour GT, Bruker).

As outer continuous phase mineral oil (M5904; Sigma-Aldrich) is used. As the inner aqueous phase, a mixture of deionized water (33% [v/v]) and glycerol (67% [v/v]; Sigma-Aldrich) is used, in which fluorescein was added to a final concentration of 200 µM. The surface tension of the two fluids is measured with a pendant drop tensiometer (Teclis Scientific). A glass cuvette is filled with oil and surfactant, while a syringe was filled with millipore water. The volume is chosen such that the pendant drop reaches an equilibrium state without detaching. The dielectric constant is measured by impedance spectroscopy (Impedance Analyzer 7260; Materials Mates). The impedance analyzer is connected to a fluid cell that contains two opposed platinum electrodes (10 mm × 10 mm) spaced at a distance of 10 mm. The cell is filled with the formulation, and a frequency scan from 1 to 10 MHz with 5 V applied is performed. The measurements are corrected with an open and closed circuit measurement to account for the impedance of the equipment, and the average over the frequency scan is taken as a dielectric constant. The viscosity of the fluids is measured with a rotational rheometer (Discovery HR-2 rheometer) with a cone (diameter: 40 mm; truncation: 55 µm; angle: 1 degree 59 min 10 s) at 20°C. The shear rate during the measurements was stepwise increased from 1 to 100 $s^{-1}$. The properties of the formulations are summarized in Table 1.

The flow in the microfluidic channels is controlled using syringe pumps (neMESYS; Cetoni). The devices are connected to flow controllers using PTFE tubing (Fischer Scientific) with an inner diameter of 0.56 mm and an outer diameter of 1.07 mm.

The microfluidic chip is placed on the stage of an inverted microscope (IX71; Olympus). The device is visualized with a high-speed camera (v210; Phantom). The laser (473 nm wavelength; Cobolt) is guided toward the sample and focused on the microfluidic channel by a microscope objective (×40; Olympus). The emitted fluorescent light from the droplets is filtered and guided toward a photomultiplier tube (H9656-20; Hamamatsu), where it is recorded. Supporting Information: Figure S2 shows a detailed schematic of the optical setup.

The electrodes on the chip are manufactured by heating the chip to 120°C and inserting low-temperature melting solder (Indium Corp.) into the electrode channels. Short electric wires are inserted in the inlets of the electrode channel to ensure a connection, after which the wires are strengthened by UV-curable glue (Loctite AA 352; Henkel). The downstream electrodes are grounded while the upstream electrodes are actuated. The voltage applied to the electrodes is controlled by a frequency generator (33210 A; Agilent) and amplified 1000 times (623B; Trek). The carrier frequency $f_{carry}$ of the modulated electric signal is 30 kHz. Data acquisition (DAQ) of the PMT signals and control of the frequency generator is automated and performed by a DAQ card (National Instruments) which executed an in-house built software (Labview 2014; National Instruments). The PMT signal is recorded for 5 s for each setting. The sampling rate of the system is 193 kHz.

**TABLE 1** Material properties of the fluids used in the experiments

| Fluid | Density $\rho$ (kg/m$^3$) | Dynamic viscosity $\eta$ (mPa·s) | Dielectric constant $\varepsilon_r$ (−) | Surface tension[a] $\gamma_0$ (mN/m) |
|---|---|---|---|---|
| Mineral oil | 840 | 30.7 | 2.2 | - |
| Glycerol:Water (0.67:0.33) | 1173 | 25.4 | 63.1 | 33 |

[a]The reported surface tension is the surface tension with mineral oil.

Matlab R2018a is used for all postprocessing steps of the recorded signals. First, the Fourier transform of the signals is calculated. Afterward, deconvolution of the Fourier transform into a background, and a peak signal is done using the frequency spectrum from 0 to 12 kHz for the background signal $a_0$. To compute $a_p$, $\delta(f_{pert})$ is defined as the maximum value in the interval $[f_{pert} - 50\,Hz, f_{pert} + 50\,Hz]$ for each experimental run. Fitting is performed using the least squares method. A built-in Matlab function detected the minima for both $a_0$ and $a_p$ in the interval [0 1]. Detection of peaks in the PMT signal is done by a built-in Matlab function with the threshold for peak height set to $2 \times 10^{-2}$ V and the threshold for peak width set to $10^{-6}$ s. Normalized histograms of the peak width distribution are compiled with a bin number $n = 400$. A Gaussian curve is fit using the least squares method, with the maximum number of function evaluations $5 \times 10^4$ and the maximum number of iterations $10^4$.

## ACKNOWLEDGMENTS

Jean-Christophe Baret acknowledges the support of the "Région Nouvelle Aquitaine." This project has received funding from the European Union's Horizon 2020 research and innovation program under the Marie Sklodowska-Curie grant agreement No. 813786.

## CONFLICT OF INTEREST STATEMENT

The authors declare no conflict of interest.

## ORCID

*David Van Assche* http://orcid.org/0000-0001-6417-8228
*Thomas Beneyton* http://orcid.org/0000-0003-2322-4886
*Jean-Christophe Baret* http://orcid.org/0000-0003-2048-8317

## REFERENCES

1. Macosko EZ, Basu A, Satija R, et al. Highly parallel genome-wide expression profiling of individual cells using nanoliter droplets. *Cell*. 2015;161:1202-1214.
2. Baret J-C, Beck Y, Billas-Massobrio I, Moras D, Griffiths AD. Quantitative cell-based reporter gene assays using droplet-based microfluidics. *Chem Biol*. 2010;17:528-536.
3. Agresti JJ, Antipov E, Abate AR, et al. Ultrahigh-throughput screening in drop-based microfluidics for directed evolution. *Proc Natl Acad Sci USA*. 2010;107:4004-4009.
4. Obexer R, Pott M, Zeymer C, Griffiths AD, Hilvert D. Efficient laboratory evolution of computationally designed enzymes with low starting activities using fluorescence-activated droplet sorting. *Protein Eng Des Sel*. 2016;29:355-366.
5. Miller TE, Beneyton T, Schwander T, et al. Light-powered $CO_2$ fixation in a chloroplast mimic with natural and synthetic parts. *Science*. 2020;368:649-654.
6. Deshpande S, Caspi Y, Meijering AEC, Dekker C. Octanol-assisted liposome assembly on chip. *Nat Commun*. 2016;7:10447.
7. Deng N-N, Yelleswarapu M, Zheng L, Huck WTS. Microfluidic assembly of monodis-perse vesosomes as artificial cell models. *J Am Chem Soc*. 2017;139:587-590.
8. Miller OJ, Harrak AE, Mangeat T, et al. High-resolution dose–response screening using droplet-based microfluidics. *Proc Natl Acad Sci USA*. 2012;109:378-383.
9. Churski K, Kaminski TS, Jakiela S, et al. Rapid screening of antibiotic toxicity in an automated microdroplet system. *Lab Chip*. 2012;12:1629-1637.
10. Marre S, Jensen KF. Synthesis of micro and nanostructures in microfluidic systems. *Chem Soc Rev*. 2010;39:1183-1202.
11. Duncanson WJ, Zieringer M, Wagner O, et al. Microfluidic synthesis of monodisperse porous microspheres with size-tunable pores. *Soft Matter*. 2012;8:10636-10640.
12. Mao AS, Shin JW, Utech S, et al. Deterministic encapsulation of single cells in thin tunable microgels for niche modelling and therapeutic delivery. *Nat Mater*. 2017;16:236-243.
13. Cramer C, Fischer P, Windhab EJ. Drop formation in a co-flowing ambient fluid. *Chem Eng Sci*. 2004;59:3045-3058.
14. Thorsen T, Roberts RW, Arnold FH, Quake SR. Dynamic pattern formation in a vesicle-generating microfluidic device. *Phys Rev Lett*. 2001;86:4163-4166.
15. Mittal N, Cohen C, Bibette J, Bremond N. Dynamics of step-emulsification: from a single to a collection of emulsion droplet generators. *Phys Fluids*. 2014;26:082109.
16. Li Z, Leshansky AM, Pismen LM, Tabeling P. Step-emulsification in a microfluidic device. *Lab Chip*. 2015;15:1023-1031.
17. Anna SL, Bontoux N, Stone HA. Formation of dispersions using "flow focusing" in microchannels. *Appl Phys Lett*. 2003;82:364-366.
18. Dreyfus R, Tabeling P, Willaime H. Ordered and disordered patterns in two-phase flows in microchannels. *Phys Rev Lett*. 2003;90:144505.
19. Garstecki P, Gitlin I, DiLuzio W, Whitesides GM, Kumacheva E, Stone HA. Formation of monodisperse bubbles in a microfluidic flow-focusing device. *Appl Phys Lett*. 2004;85:2649-2651.
20. Baret J-C, Miller OJ, Taly V, et al. Fluorescence-activated droplet sorting (FADS): efficient microfluidic cell sorting based on enzymatic activity. *Lab Chip*. 2009;9:1850-1858.
21. Abate AR, Weitz DA. High-order multiple emulsions formed in poly (dimethylsiloxane) microfluidics. *Small*. 2009;5:2030-2032.
22. Cubaud T, Mason TG. Capillary threads and viscous droplets in square microchannels. *Phys Fluids*. 2008;20:053302.
23. Utada AS, Fernandez-Nieves A, Stone HA, Weitz DA. Dripping to jetting transitions in coflowing liquid streams. *Phys Rev Lett*. 2007;99:094502.
24. Plateau J. I. Experimental and theoretical researches on the figures of equilibrium of a liquid mass withdrawn from the action of gravity. *Phil Mag Sci*. 1857;14:1-22.
25. Rayleigh L. On the instability of jets. *Proc London Math Soc*. 1878;s1-10:4-13.
26. Utada AS, Fernandez-Nieves A, Gordillo JM, Weitz DA. Absolute instability of a liquid jet in a coflowing stream. *Phys Rev Lett*. 2008;100:014502.
27. Guillot P, Colin A, Utada AS, Ajdari A. Stability of a jet in confined pressure-driven biphasic flows at low reynolds numbers. *Phys Rev Lett*. 2007;99:104502.
28. Guillot P, Colin A, Ajdari A. Stability of a jet in confined pressure-driven biphasic flows at low Reynolds number in various geometries. *Phys Rev E*. 2008;78:016307.
29. Rohani M, Jabbari F, Dunn-Rankin D. Breakup control of a liquid jet by disturbance manipulation. *Phys Fluids*. 2010;22:107103.
30. Cordero ML, Gallaire F, Baroud CN. Quantitative analysis of the dripping and jetting regimes in co-flowing capillary jets. *Phys Fluids*. 2011;23:094111.
31. Jaworek A. Micro-and nanoparticle production by electrospraying. *Powder Technol*. 2007;176:18-35.
32. Wei C, Qin H, Chiu C-P, Lee Y-S, Dong J. Drop-on-demand E-jet printing of con- tinuous interconnects with AC-pulse modulation on highly insulating substrates. *J Manufact Syst*. 2015;37:505-510.
33. Gu H, Malloggi F, Vanapalli SA, Mugele F. Electrowetting-enhanced microfluidic device for drop generation. *Appl Phys Lett*. 2008;93:183507.
34. Tan SH, Semin B, Baret J-C. Microfluidic flow-focusing in AC electric fields. *Lab Chip*. 2014;14:1099-1106.

35. Tan S, Maes F, Semin B, Vrignon J, Baret J-C. The microfluidic jukebox. *Sci Rep*. 2014;4:4787.
36. Castro-Hernández E, García-Sánchez P, Tan SH, Gañán-Calvo AM, Baret JC, Ramos A. Breakup length of AC electrified jets in a microfluidic flow-focusing junction. *Microfluid Nanofluid*. 2015;19:787-794.
37. Castro-Hernández E, García-Sánchez P, Alzaga-Gimeno J, Tan SH, Baret JC, Ramos A. AC electrified jets in a flow-focusing device: jet length scaling. *Biomicrofluidics*. 2016;10:043504.
38. Lippmann GM. Relation entre les phenomenes electriques et capillaires. *Ann Chim Phys*. 1875;5:494-549.
39. Eggers J, Villermaux E. Physics of liquid jets. *Rep Prog Phys*. 2008;71:036601.
40. Castro-Hernández E, García-Sánchez P, Velencoso-Gómez A, et al. Droplet group production in an AC electro-flow-focusing microdevice. *Microfluid Nanofluid*. 2017;21:158.
41. Brosseau Q, Vrignon J, Baret J-C. Microfluidic dynamic interfacial tensiometry. *Soft Matter*. 2014;10:3066-3076.
42. Riechers B, Maes F, Akoury E, Semin B, Gruner P, Baret JC. Surfactant adsorption kinetics in microfluidics. *Proc Natl Acad Sci USA*. 2016;113:11465-11470.
43. Schmid L, Franke T. SAW-controlled drop size for flow focusing. *Lab Chip*. 2013;13:1691-1694.
44. Franke T, Braunmüller S, Schmid L, Wixforth A, Weitz DA. Surface acoustic wave actuated cell sorting (SAWACS). *Lab Chip*. 2010;10:789-794.
45. Duffy DC, McDonald JC, Schueller OJA, Whitesides GM. Rapid prototyping of microfluidic systems in poly(dimethylsiloxane). *Anal Chem*. 1998;70:4974-4984.

## SUPPORTING INFORMATION

Additional supporting information can be found online in the Supporting Information section at the end of this article.

**How to cite this article:** Van Assche D, Beneyton T, Baret J-C. Rectifying jet breakup by electric forcing. *Droplet*. 2023;2:e45. doi:10.1002/dro2.45